Dual Infrared 2-Photon Microscopy Achieves Minimal Background Deep Tissue Imaging in Brain and Plant Tissues

Mohammad M. Safaee, Shoichi Nishitani, Ian R. McFarlane, Sarah J. Yang, Ethan Sun, Sebastiana M. Medina, Henry Squire, and Markita P. Landry*

Traditional deep fluorescence imaging has primarily focused on red-shifting imaging wavelengths into the near-infrared (NIR) windows or implementation of multi-photon excitation approaches. Here, the advantages of NIR and multiphoton imaging are combined by developing a dual-infrared two-photon microscope that enables high-resolution deep imaging in biological tissues. This study first computationally identifies that photon absorption, as opposed to scattering, is the primary contributor to signal attenuation. A NIR two-photon microscope is constructed next with a 1640 nm femtosecond pulsed laser and a NIR PMT detector to image biological tissues labeled with fluorescent single-walled carbon nanotubes (SWNTs). Spatial imaging resolutions are achieved close to the Abbe resolution limit and eliminate blur and background autofluorescence of biomolecules, 300 µm deep into brain slices and through the full 120 µm thickness of a *Nicotiana benthamiana* leaf. NIR-II two-photon microscopy can also measure tissue heterogeneity by quantifying how much the fluorescence power law function varies across tissues, a feature this study exploits to distinguish Huntington's Disease afflicted mouse brain tissues from wildtype. These results suggest dual-infrared two-photon microscopy can accomplish in-tissue structural imaging and biochemical sensing with a minimal background, and with high spatial resolution, in optically opaque or highly autofluorescent biological tissues.

M. M. Safaee, S. Nishitani, I. R. McFarlane, S. J. Yang, E. Sun,
S. M. Medina, H. Squire, M. P. Landry
Department of Chemical and Biomolecular Engineering
University of California
Berkeley, CA 94720, USA
E-mail: landry@berkeley.edu
M. P. Landry
Innovative Genomics Institute (IGI)
Berkeley, CA 94720, USA
M. P. Landry
California Institute for Quantitative Biosciences
QB3
University of California
Berkeley, CA 94720, USA
M. P. Landry
Chan-Zuckerberg Biohub
San Francisco, CA 94158, USA

The ORCID identification number(s) for the author(s) of this article can be found under https://doi.org/10.1002/adfm.202404709

1. Introduction

Fluorescence imaging within highly absorbing and scattering biological tissues is critical for biomedical and bioengineering applications to visualize fundamental biological functions and structures.[1–3] New techniques that enable imaging in dense biological tissues are needed, particularly for imaging in tissues with high absorbance and scattering properties, or in which endogenous visible autofluorescence interferes with imaging.[4,5] The use ubiquity and spatiotemporal resolution of fluorescence microscopy have been advantageous over non-fluorescence approaches such as ultrasound imaging, computed tomography (CT) scan, and magnetic resonance imaging (MRI).[6] While fluorescence microscopy is the most ubiquitous imaging technique, imaging in highly absorbing and scattering tissues continues to be a challenge for the field of bioimaging.[1–8] Scattering and absorption of emitted photons are the two most important parameters that determine the imaging depth and spatial resolution of fluorescently tagged biological structures in fluorescence imaging, though their relative contributions to signal attenuation is not well known.[8] Scattering has been demonstrated to inversely depend on the emission wavelength, while absorption is substantially affected by endogenous biomolecules, notably water, hemoglobins, and plant pigments.[9] Water molecules show significant absorption in the near-infrared (NIR) regions of 1400−1500 and >1700 nm due to vibrational overtones.[9] Hemoglobin molecules, the most abundant chromophores in mammals, intensely absorb visible emission photons with multiple absorption bands extending through ≈650 nm.[9] Furthermore, the presence of autofluorescing biomolecules such as flavins, porphyrins, and collagens in major mammalian internal organs and fluids, and chlorophyll pigments in plants, also results in autofluorescence in the visible window, making it difficult to perform fluorescence imaging in this region.[9]

One approach that particularly enhances fluorescence imaging depth and spatial resolution is the design of microscopes that minimize optical scattering and absorption.[4,5,10] Traditional fluorescence imaging employs single-photon excitation, wherein

**ADVANCED
SCIENCE NEWS**

www.advancedsciencenews.com

**ADVANCED
FUNCTIONAL
MATERIALS**

www.afm-journal.de

one excitation photon of high energy excites the fluorophore, usually by raising an electron to a higher energy level followed by exciton relaxation in which a photon of lower energy is emitted, usually from an electron radially decaying to a lower energy state.[9,11,12] In multiphoton excitation, which includes two, three, and four photon excitation, multiple lower energy photons arrive at the fluorophore nearly simultaneously to excite the fluorophore in a way that mimics single photon excitation and results in anti-Stokes fluorescence emission that increases quadratically with the power density of the excitation.[5,12] To increase the likelihood of simultaneous photon excitation, multiphoton microscopes commonly employ pulsed lasers with the beam focused to a diffraction-limited spot, increasing the density of excitation photons within an excitation volume. This excitation volume is then scanned through the sample to collect an image.[13] The benefits of multiphoton microscopy over conventional single-photon microscopy are threefold: 1) the excitation light is of longer wavelength and thus decreases the amount of scattering, increasing the maximal imaging depth 2) the simultaneity requirement limits the out-of-plane excitation (and thus emission), lowering background counts and increasing the signal to noise ratio (SNR) 3) the limited excitation volume allows for z-sectioning and, given enough time, 3D-imaging. The detriments of multiphoton imaging are twofold: 1) imaging is slow as rastering for image acquisition takes time, though with bright signal and appropriate hardware this can be mitigated and 2) multiphoton excitation is dimmer than single-photon excitation due to the simultaneity requirement, yet this can be mitigated with the use of powerful lasers with shorter (denser) pulses. The interplay of these factors – imaging depth and spatial resolution – remains difficult to predict, particularly due to a dearth of fluorophores that can emit in the near-infrared wavelengths deemed optimal for imaging in biological tissues.[14] To-date, multiphoton microscopy has achieved excellent imaging quality across biological specimens, however, the emission wavelengths of previously-reported multiphoton microscopes have been confined to the visible regime. In this work, we develop a two-photon imaging microscope with near-infrared excitation *and* emission channels and support this approach with Monte Carlo simulations suggesting that photon absorption, as opposed to scattering, is the primary contributor to signal attenuation.

Orthogonal to the benefits of multiphoton excitation, selecting fluorophores that enable fluorescence imaging with minimal photon absorption and scattering is beneficial.[1,15–17] In particular, the dearth of emission photons relative to laser-based excitation photons makes the former particularly important to optimize. Despite the potential contribution of NIR-fluorescent emission photons, this approach has remained less explored than optimizing the power law of photoexcitation. Specifically, shifting both excitation and emission into the NIR window, particularly in the long NIR region (1.0–1.7 µm, termed as NIR-II window), could be critical to enhancing the imaging depth and minimizing the tissue scattering, absorption, and autofluorescence.[9] Quantum-dots (QDs)[18,19] and single-walled carbon nanotubes (SWNTs)[20–24] are among the few fluorescent agents in the NIR-I and NIR-II windows, respectively, that have recently been utilized for in vivo single photon fluorescence imaging of mice inner organs such as liver, spleen, blood vessels in the hindlimb and cerebral vasculatures in brain. Although two-photon excita-

tion has been previously utilized to image fluorophores in visible and NIR-I windows, there has been no report of two-photon NIR-II fluorescence imaging in either in vitro or in vivo settings.[25–29]

Herein, we first produced Monte Carlo simulations to elucidate the effect of various optical parameters on the emission light escaping from absorbing and scattering media and find that photon absorption far more greatly impacts imaging quality than emission light scattering. We therefore identified maximum transmission windows of 900–1300 and 1550–1800 nm within the NIR-II region and constructed a dual NIR-II excitation-emission two-photon microscope, employing a femtosecond 1640 nm erbium laser as a source of excitation photons and chiral SWNTs fluorescing between 900 and 1200 nm as a source of emission photons. To validate the two-photon excitation of this microscope, we varied the power of the excitation beam and quantified the fluorescence intensity of SWNT fluorophores immobilized in an agarose hydrogel. The dependence of the intensity on the excitation beam power was fitted with a power law function with powers ranging from 1 to 2 at various fluorescent regions of interest (ROIs), indicating the fact that SWNTs were heterogeneously dispersed in the gel matrix and formed aggregates. Utilizing QDs immobilized on a glass slide, the radial and axial resolutions of the NIR-II two-photon microscope were calculated to be 0.92 and 6 µm. To validate the system's ability to image biological samples, we labeled brain slices and plant leaves with SWNT emitters and imaged these samples under two-photon excitation. We observed a significant improvement in the blur and depth of the imaging quality achieved with NIR-II two-photon imaging compared to previous single photon imaging systems. Furthermore, we leveraged the association between power law and SWNT aggregation to successfully differentiate Huntington's Disease (HD) from wild type (WT) brain slices, the former of which exhibits greater tissue heterogeneity and therefore increased SWNT aggregation.

2. Results and Discussion

2.1. Monte-Carlo Simulations Suggest a Microscopy Approach that Minimizes Photon Absorption

To understand the greatest limiting factors in detecting fluorescence from deep in tissue, we first conducted a series of Monte Carlo simulations to understand the theoretical fate of photons from their departure from the laser through their re-collection by the objective from a fluorescent specimen and reaching a detector (**Figure 1a** and Equations (1)–(3)). We then implemented this Monte-Carlo simulation framework to study the collection efficiency of post-fluorescence emission light, taking into account tissue absorption (μ_A), tissue scattering (μ_S), tissue depth of focus (D), in addition to the numerical aperture (NA) and working distance (WD) of the objective. The simulation generates photons at the microscope focal point while randomly scattering these photons post-emission based on tissue scattering anisotropy, and records the total distance traveled by these photons. While photons exit the media in which they are being "imaged", the data is saved only if the photon exit trajectory would intercept the objective and at an angle of incidence within a defined range that would allow the photon to be recovered into the objective in a
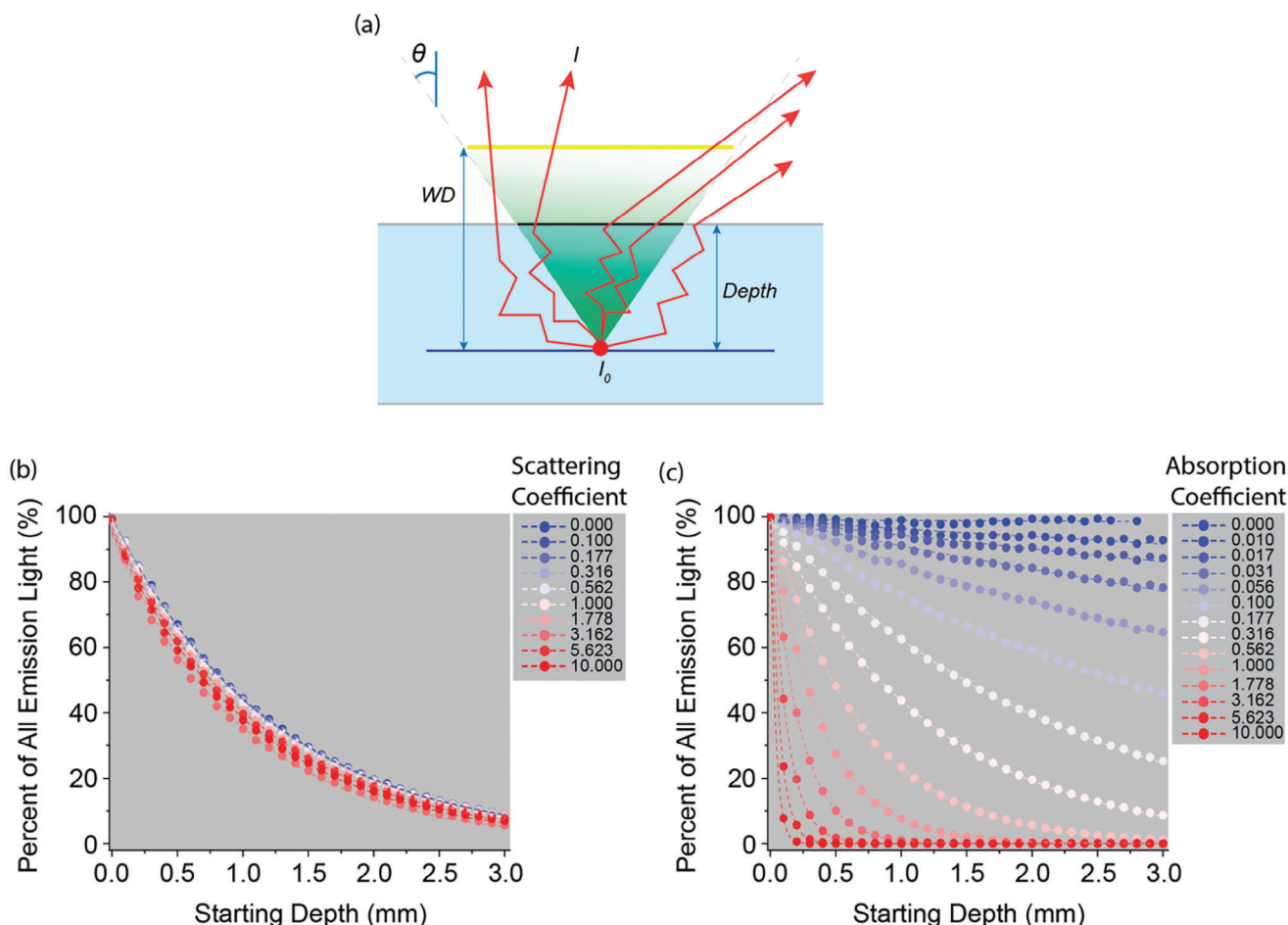
**ADVANCED
SCIENCE NEWS**

www.advancedsciencenews.com

**ADVANCED
FUNCTIONAL
MATERIALS**

www.afm-journal.de

Figure 1. Monte Carlo simulations to preditct the effect of various parameters on the emission signal. a) Schematic of Monte Carlo simulation for photon fate when imaged with two-photon microscopy in biological tissues. Photons are generated at the point of focus while randomly scattering based on the media scattering anisotropy and exiting the medium. Simulated detection of the photons requires photon arrival at the objective at an angle shallower than $\theta = sin^{-1}$ (NA/n). As an example, the leftmost two emission photons both encounter the objective at an angle shallower than θ. The middle photon encounters the objective but does so at so steep an angle it impacts the side of the objective or light path and will not reach the detector. As such, our estimates of imaging light collected are conservative. b,c) Simulations of our 0.95 NA and 2.5 mm WD objective show that the effect of photon scattering on emission light is minimal when compared to the effects of absorption.

realistic setting – in other words, photons that are successfully emitted from the "imaged" tissue but that hit the objective at an acute angle are considered unsuccessful at reaching the detector. The output of simulations from Equation (3) shows no measurable effect of WD on the emission light passed through non-absorbing and non-scattering media, although as expected, increasing the NA increases the percent of emission light collected (Figure S1a, Supporting Information). Figure S1b (Supporting Information) shows our simulations successfully reproduce the theoretical effects of WD and NA in non-absorbing and non-scattering media, observed in Equation (3), within a margin of ±0.001 percent.

$$I = I_0 \, \varepsilon_{Objective} 10^{-\mu z} \tag{1}$$

$$\varepsilon_{Objective} = \frac{1 - \sqrt{1 - \left(\frac{NA}{n}\right)^2}}{2} \tag{2}$$

$$\frac{I}{I_0} \approx \varepsilon_{Objective} = \frac{1 - \sqrt{1 - \left(\frac{NA}{n}\right)^2}}{2} \tag{3}$$

To interrogate the effect of these parameters in absorbing and scattering media, we plotted the simulated emission signal as function of depth, for every NA and WD, while varying either μ_A or μ_s and holding the other variable constant. We then fit each simulated trend over varying depths to the form $P_{PD} = P_0 \, 10^{-az}$. Here, P_{PD} represents the percent of photons detected, P_0 represents the initial number of photons emitted from the fluorescent point-source, a is a scaling factor, and z represents the imaging depth of the sample. The scaling factor (a) was fit linearly versus μ_A and μ_S, $a = m\mu_x + b$, where the slope of the line (m) can determine the degree of absorbance and scattering contributions to the emission light. Averaging these slopes over all other variables indicates $m_A = 1.217 \pm 0.078$, showing that
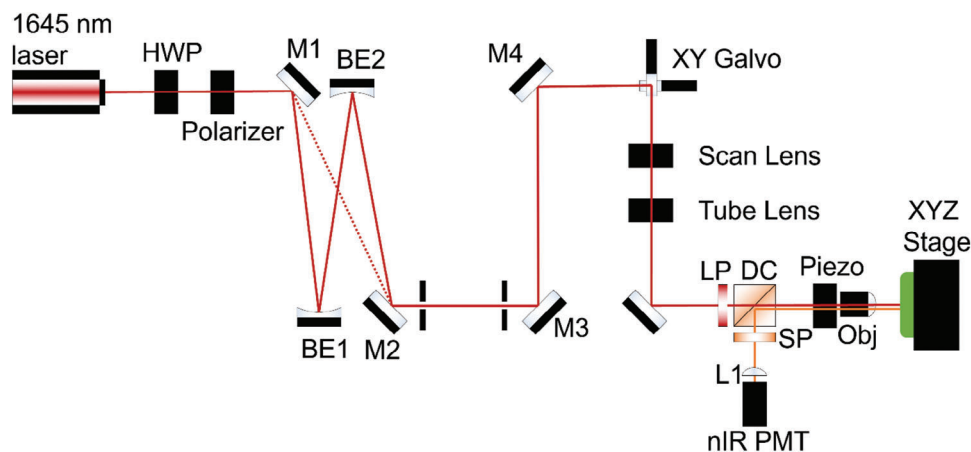
Figure 2. Schematic of the NIR-II two-photon microscope. Schematic of the dual NIR excitation-emission two-photon microscope for imaging through highly scattering media. Mirror pairs M1:M2 and M3:M4 are used to align the left and right halves of the light path, respectively, to the two alignment apertures between M2 and M3. M1 can be adjusted to bypass the beam expansion mirrors. BE: beam expander, LP: 1500 nm longpass filter, SP: 1500 nm shortpass filter, DC: dichroic mirror comprising 1500 longpass and 850 nm shortpass, Objective: 20x Lieca, with 2.0 mm working distance and numerical aperture of 0.95.

P_{PD} varies significantly as a function of the absorption properties of the imaged media. In contrast, we find that the average slope for μ_S is $m_S = 0.009 \pm 0.002$, indicating that P_{PD} varies little as the scattering properties of the imaged media are changed. These results show that the effect of absorption (μ_A) on percent of photons detected (P_{PD}) in near-infrared fluorescence microscopy is far greater than that of scattering (μ_S) at all imaging depths (Figure 1b,c). Equation 4 represents the effect of all parameters in our six-dimensional model on the simulated percent of detected photons.

$$I\left(\mu_A, \mu_S, NA, WD, z\right) = I_0 \cdot 10^{-\left(m_A\mu_A + m_S\mu_S\right)z} \tag{4}$$

where $m_A = 1.217 \pm 0.078$ and $m_S\ 0.009 \pm 0.002$

Thus, the weight of μ_A ($m_A = 1.217$) is roughly 135 times larger than the weight of μ_S ($m_S = 0.009$), supporting a two-photon microscope design principle in which the focus is on decreasing loss of power on the excitation beam and designing the microscopy hardware and imaging experiments around the high cost of signal loss arising from the absorption properties of the imaging media, and less so around the relatively minimal cost arisen from its scattering properties.

Therefore, the selection of both excitation and emission windows in NIR-II regions, where there is minimal absorption by water and biomolecules, is critical to minimize signal attenuation and background in dense biological tissues. Due to substantial photon absorption of water molecules in the ≈1400–1500 nm range and biological molecules in visible and NIR-I windows, we identified maximal photon transmission to occur at 900–1300 and 1550–1800 nm. To achieve excitation and emission within these windows, a laser with a longer wavelength that can effectively excite fluorophores in the NIR-II region should be selected. Such a combination can be achieved with a 1640 nm excitation laser and NIR-II SWNT emitters which will together operate in wavelength ranges optimal for minimization of photon absorption in biological media.[30]

2.2. Microscope Design Allows Imaging Near Abbe Resolution Limit

Based on our Monte Carlo simulations, we constructed a dual infrared microscope that minimizes the contribution of media absorption properties and in which both excitation and emission channels are within the tissue transparency maxima (**Figure 2**). The microscope was designed to maximize the imaging depth with NIR-II emitters such as SWNTs, or other NIR fluorophores, while utilizing two-photon excitation. To this end, we used a 1640 nm laser (IMRA America, Inc, model HX-150). To tune the laser power, a 1550 nm zero-order half-wave plate (HWP) and mounted Glan laser polarizer are used. The HWP is actuated by a motorized precision rotation stage providing a minimum incremental motion of 25 arcsecond over the 360° rotation with a 2 arcsecond resolution. The beam is expanded using a pair of silvered mirrors to avoid chromatic effects of transmissive lenses. The scanning galvo is a pair of 5 mm mirror single axis galvanometer scanner (Edmund Optics model 11–762 – 6210H) with a 60-degree scan angle. Scan lens and tube lens further expand the beam and correct wavefront distortion from the scanning mirrors. The excitation light transmits through a dichroic mirror which reflects the emission light (850–1500 nm) to the detector. The objective was selected to successfully transmit NIR light while maximizing NA (tightening the spatial resolution of the excitation volume). All data presented is while using a Lecia Microsystems objective with 0.95 NA and 2.5 mm WD. Emission light is not descanned[28] and is focused directly onto a Hamamatsu H10330C-25-C2 near-infrared PMT detector sensitive to 950–1400 nm light. We use two scanning patterns for data acquisition: raster scanning and circular scanning. Raster scanning is performed to collect all images, targeting a full rectangle of equally spaced grid of pixels. Circular scanning targets a series of pixels along the circumference of a circle repeatedly sampling a wide range of locations. This latter mode specially facilitates faster data acquisition while finding the focus or collecting the raw fluorescence intensities is desired rather than acquiring

**ADVANCED
SCIENCE NEWS**

www.advancedsciencenews.com

**ADVANCED
FUNCTIONAL
MATERIALS**

www.afm-journal.de

full images. To control the microscope hardware, data acquisition and image processing, an object-oriented software was constructed and developed in house using LabVIEW. This software is comprised of multiple classes, with a core class being the most generic class and a variety of specific classes for the microscope hardware including motion axes, laser shutter, power meter and detector. Every class runs based on a JKI state machine that calls various public, protected, and private methods (Figure S2, Supporting Information).

2.3. Microscope Characterization Using NIR-Emitting SWNTs Verifies Two-Photon Excitation and Reveals Relationship Between SWNT Aggregation and Power Law Order

As the greatest advantage of two-photon imaging is shifting the excitation and emission bandwidths to longer wavelengths in the NIR, selecting fluorophores that enable excitation that minimizes absorption within the NIR-II window will enable NIR imaging within tissues with minimal background contributions. Photostable NIR emitters are rare, despite their potential utility for deep-tissue imaging. To achieve emission in the NIR, emitters with intramolecular π-conjugated systems and substituent electronic effects are needed. Standard high energy absorption and emission (300–600 nm) is attributed to $\pi-\pi^*$ and n–π^* transitions of conjugated structures, while lower energies (600–1700 nm) emanate from intramolecular charge transfer between peripheral donors.[31] In this work, we draw upon two NIR emitters for calibration of our microscope and to demonstrate its potential for two-photon NIR-I and NIR-II imaging: SWNTs and NIR QDs.

Due to properties gained at the quantum level, various chiralities of SWNTs are comprised of SP^2 carbon atoms in a single graphitic layer rolled up along a chiral vector into a nanocylinder.[9,32] The quantum confinement along the radial direction of the SWNTs results in extremely sharp maxima of electronic density of states.[32] Due to the lack of density of states at the Fermi level for semiconducting SWNTs, their electronic bandgap energies result in various chiralities that exhibit distinct narrow bandwidth fluorescence in the NIR-II window.[9,32] Despite generally low optical quantum yield ranging from 2% to 7%,[33] SWNTs fluorescence is exceptionally photostable and responds to perturbations in its local dielectric environment, making them ideal candidates for a wide range of biological imaging[11,12] and sensing[34–37] applications. Moreover, their nanometer-scale dimensions and fast optical response times enable extraordinary spatiotemporal resolution to visualize synaptic-scale neurotransmitter release in brain tissue. As for their bioimaging applications, SWNTs have been extensively utilized as fluorophores for conventional single-photon imaging[38] as well as confocal[39] and up-conversion imaging[40]; however, their application in two-photon imaging has not been explored. The existence of numerous SWNT chiralities with bandgap energies in the NIR-II window can further enable the development of two-photon excitation modalities with enhanced imaging depth and optical sectioning qualities in optically opaque tissues such as the brain, and highly autofluorescing samples such as plant leaves. We therefore assess whether introducing two-photon excitation in combination with NIR fluorophores such as SWNTs

can enable dual-infrared fluorescence microscopy in such biological tissue samples.

To confirm that the photoexcitation process of our constructed microscope indeed occurs through two-photon excitation, we prepared a surfactant-coated multi-chirality HiPco SWNT sample and quantified the dependence of its fluorescence intensity on excitation laser power. We utilized surfactant-coated HiPco SWNT due to their colloidal stability, and their well-characterized photoluminescence properties.[41,42] Theoretical work has predicted that fluorescence emission is a power law function of the excitation beam power, $I_{em} \sim P^n$, where P is the power of the excitation light and n is a fitted coefficient. While two-photon excitation systems are expected to follow a power law of order 2,[28,43] we found the measured emission signal in relation to the excitation power follows a power law of order 1.66 for surfactant-coated SWNTs in the solution phase (**Figure 3a**). To better mimic the imaging conditions in biological tissues, where the SWNTs are localized within various ROIs in the tissue structure, we repeated the above power-law study with SWNTs immobilized in a 5% agarose hydrogel and observed a range of stable power dependencies for each SWNT ROI ranging from 1 to 2 (Figure 3b). Our solution-phase and immobilized-SWNT experiments suggest that the solution-phase power law dependence is slightly below the predicted power of 2, and the surface-immobilized experiments suggests endogenous variability in individual SWNT sample power law dependence. It has been previously proposed that power laws <2 are the result of chromophore saturation, whereby the majority of fluorophores have been excited and subsequent increases in emission are due to expanding the excitation volume rather than improving the excitation efficiency.

It is also possible that the observed power law discrepancy was due to our multi-chirality sample, in which each chirality exhibits a unique two-photon absorption peak and are therefore subject to off-target photoexcitation. To test this possibility, we immobilized the surfactant-coated single-chirality (6,5) SWNTs into a 5% agarose hydrogel and obtained emission intensities as a function of excitation laser power. Fitting the (6,5) SWNT data with power law functions, we again observed a range of power (n) dependencies between 1 and 2, with average power 1.39 despite testing a single-chirality sample (Figure S3a, Supporting Information).

An alternate interpretation is that imperfectly monochromatic laser light excited the fluorophore via single-photon excitation, adding a stronger linear term to the power response. To consider which of these effects are at play in our system, we used multiple strong cutoff filters (3 × 1500 long pass filters) that collectively impose a 10^{-15} reduction in excitation photons of wavelengths ranging from 600 to 1450 nm. As a result, of the total 150 mW excitation light, fewer than 450 photons are predicted to pass all filters which accounts for fewer PMT counts than we detect from dark current (4000 cps) at most. As such, single photon excitation is an unlikely contributor to our <2 power law dependence.

We hypothesize that the differential power laws in both single- and multiple-chirality SWNT samples can be attributed to either of these two factors: 1) the differential cross sections of the excited SWNT aggregates heterogeneously distributed in the gel matrix, as each SWNT has a unique photoabsorption maximum 2)
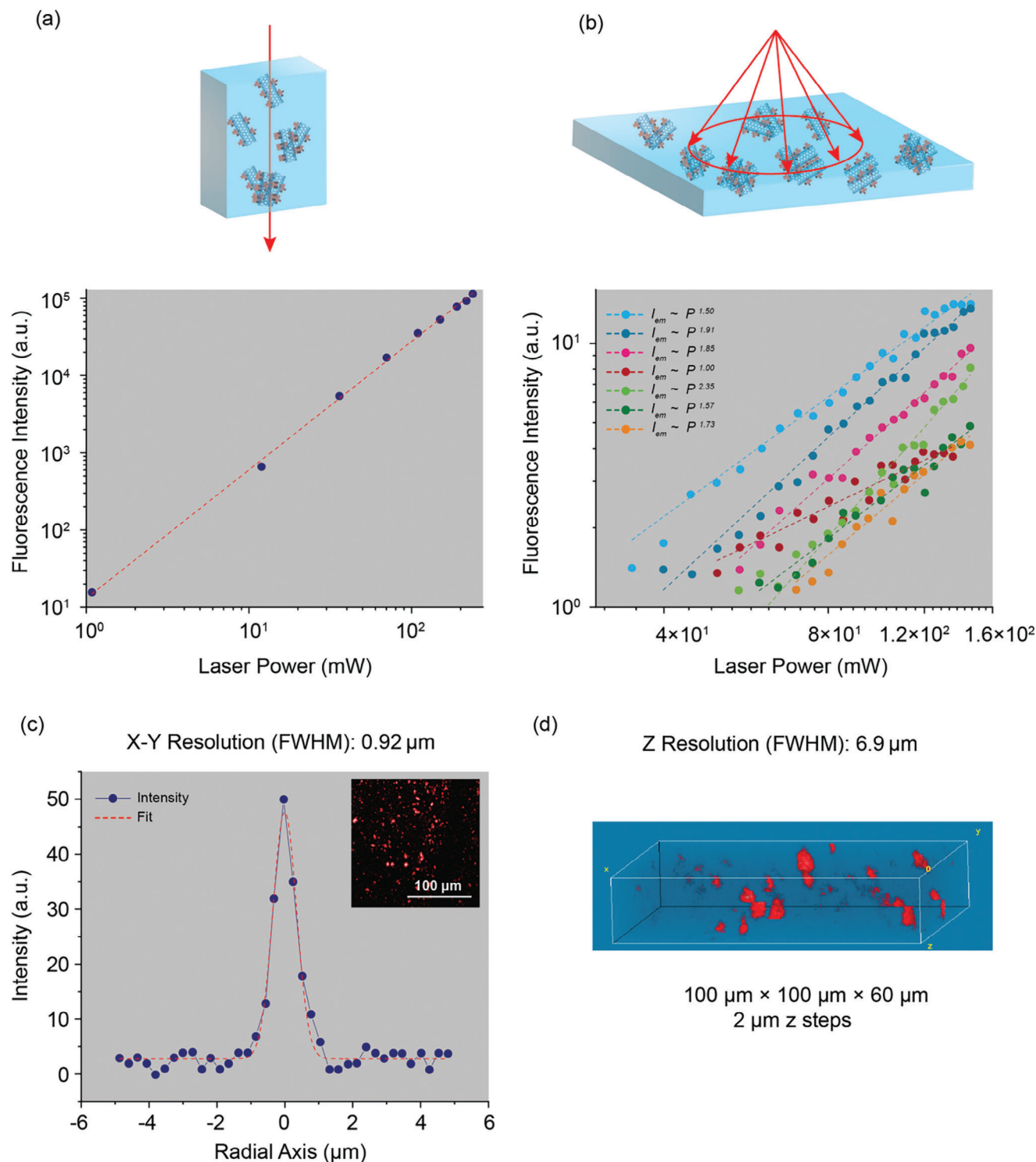
Figure 3. Power law response and resolution for SWNTs and QDs with NIR-II two-photon excitation. a) Power response for multiphoton excitation of SWNTs in solution with a collective power law of 1.66. b) Power response from various ROIs for multiphoton excitation of SWNTs incorporated into an agarose hydrogel. Power laws from the hydrogel were obtained by cyclically scanning the laser beam over a circle and range from 1 to 2, with average power-law scaling of 1.70. The resolution of the microscope is quantified from fluorescence emission profiles of NIR-emitting QDs. The full width at half maximum is c) 0.92 µm radially, and d) 6 µm axially.

**ADVANCED
SCIENCE NEWS**

www.advancedsciencenews.com

**ADVANCED
FUNCTIONAL
MATERIALS**

www.afm-journal.de

formation of SWNT aggregates of different stiffness in the gel matrix (rigid vs loose aggregates). In either case, the consistency in the range of power law distributions, many of which approach 2 (Figure 3b), suggest we are accomplishing two-photon excitation in a reasonable subset of our SWNT fluorophores. In prior work, the two-photon cross section of SWNTs with our excitation source was calculated to be 216 000 GM using DTTC as a reference fluorophore,[14] falling within the expected value range based on other prior work.[44]

As both photoabsorption cross section and SWNT degree of aggregation in the gel matrix can determine their photon absorption behavior, their power laws could be utilized to quantitatively investigate the heterogeneity of the SWNT aggregates incorporated into hydrogels, and potentially, to determine the heterogeneity of SWNT-labeled biological tissues. To examine the former, we tuned the degree of SWNT aggregation in our hydrogels by ultracentrifugation-based SWNT filtration and mixing SWNT into hydrogels prior to gel solidification, as described in Methods, such that SWNT are homogeneously cast into the gel matrix (Figure S3b, Supporting Information). Acquiring two-photon excitation power laws (Figure S3c, Supporting Information), we observe that when the SWNTs are homogeneously distributed in the gel matrix, the powers (n) possess a narrow distribution ≈1 with average value of 0.94, whereas when the SWNTs make aggregates and heterogeneously distribute in the gel matrix, the powers (n) span over a larger range between 1 and 2 with average value 1.70 (Figure S4, Supporting Information). These data suggest that SWNT-SWNT charge transfer interactions may enable two-photon excitation of the SWNT fluorophore in a manner not observed when SWNT are more singly dispersed. Furthermore, as we always observe substantial heterogeneities in SWNT-labeled biological tissues, we can expect to observe these differential powers in biological tissues as well; therefore, we predict that SWNT two-photon imaging power laws can be potentially utilized as an analytical platform to quantify the heterogeneity of biological tissues.

Next, we quantified the microscope's spatial resolution by imaging NIR QDs (PbS/CdS) on a glass surface (Fig. 3c inset). NIR QDs were selected to quantify the microscope's spatial resolution owing to the relative ease with which NIR QDs can be individually immobilized on a surface, and the easily quantifiable physical dimensions of QDs relative to length-polydisperse SWNTs. When imaging NIR QDs, the sharpest features, i.e., features that fit to gaussians with the smallest standard deviation, occurred consistently with a FWHM of 0.92 µm (Figure 3c). By focusing the microscope in the Z axis, we determined the axial resolution to be 6.0 µm (Figure 3d). This resolution compares well to the diffraction limit, calculated from Abbe resolution, of 0.92 and 6.9 µm in radial and axial dimensions respectively. Although in vivo fluorescence imaging in NIR-II with single-photon imaging has been previously achieved by developing QDs that emit in the long NIR-II range (1500–1700 nm), our two-photon NIR-II imaging technology presents a significant improvement in the radial resolution by almost an order of magnitude compared to previous work and confirms the benefits of two-photon excitation for both decreasing background and increasing spatial resolution.[3,4]

2.4. Two-Photon Imaging of SWNT-Labeled Brain Tissue Reveals Deeper Tissue Imaging and Validates Power Law Analysis to Measure Brain Tissue Heterogeneity

As mentioned previously, a key limitation for imaging biological structures in tissue lies in the photon absorption and scattering properties of biological tissues leading to attenuation of fluorescence. In particular, imaging the brain microstructure is challenging, and imaging the brain extracellular space has mostly relied on electron microscopy, which requires tissue fixation and therefore compromises the integrity of the brain extracellular space.[45,46] Indeed, recent work by Cognet and colleagues has shown that SWNT can be used to map the brain extracellular space in acute slices kept viable and spatially intact using single-photon microscopy.[47,48] To demonstrate the capabilities of our two-photon platform for imaging brain tissue, we labeled both surfaces of brain slices by co-incubating brain slices with 2 mg L^{-1} (GT)$_6$-SWNT, a SWNT nanosensor that generates the best response to dopamine,[49] and gently rinsing SWNT that had not localized into the brain tissue extracellular space, as described previously (**Figure 4a**).[11] To quantify the depth of imaging achievable with our NIR-II two-photon microscope, we prepared brain slices of two thicknesses, 300 and 500 µm, labeled both surfaces of brain slices with (GT)$_6$-SWNT, and acquired z-stack images with 20 µm step sizes, starting from the top of the brain slice and moving the microscope stage through the full slice thickness. For the 300 µm slice, we imaged the SWNT NIR signal from the slice top surface, moved the microscope through the slice, and imaged the SWNT NIR signal from the slice bottom surface, successfully collecting SWNT signal from both brain slice surfaces (Figure 4b). We also repeated this experiment with a 500 µm thick brain slice and were only able to image SWNT signal from the top-most surface of the brain slice (Figure S5, Supporting Information). These results indicate that NIR two-photon microscopy is able to image through brain tissue depths of at least 300 µm but that we lose the ability beyond that tissue thickness. In addition to imaging depth, we also explored the advantages in imaging quality provided by NIR two-photon microscopy. Specifically, we observe a substantial reduction in the blur of the images compared to the images we obtained in our previous studies using a single photon NIR microscope, confirming the advantage of two-photon excitation in enhancing the point spread function and decreasing the excitation volume (Figure S6a, Supporting Information). Additionally, single photon NIR microscopy is unable to image SWNT through a 300 µm brain slice (Figure S6b, Supporting Information), further confirming the depth uniquely achieved with two-photon NIR microscopy.

As SWNTs label brain tissue slices via diffusion and retention into the brain extracellular space,[12,47] SWNT-based brain tissue labeling is inherently stochastic. Our above results show that NIR two-photon microscopy can be used to quantify the different aggregation states of agarose gel samples labeled with SWNT. We therefore sought to assess whether two-photon NIR microscopy could be used to measure brain slice tissue heterogeneity when labeled with SWNT. The dynamic structure and spatial organization of the extracellular space in the brain is altered in neuropsychiatric and degenerative diseases[47] thus it is possible that SWNT-labeling of brain tissue and power law analysis of
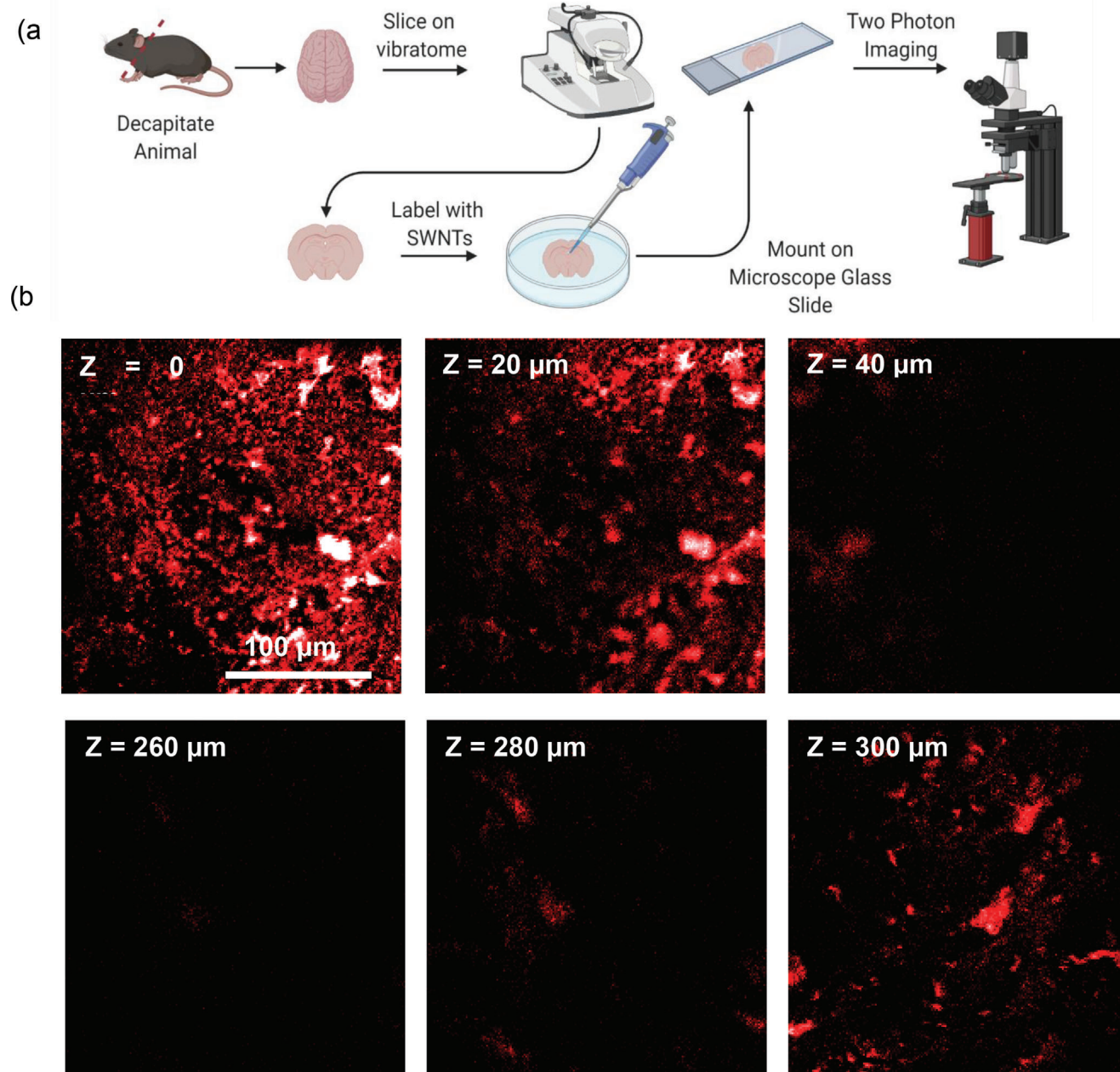
**ADVANCED
SCIENCE NEWS**

www.advancedsciencenews.com

**ADVANCED
FUNCTIONAL
MATERIALS**

www.afm-journal.de

Figure 4. NIR-II two-photon imaging of brain slices. a) Schematic representation of the dissection process for the generation of acute coronal brain slices. b) Imaging a 300 µm brain slice labeled with SWNT emitters on both slice surfaces. A z-stack was obtained with 20 µm step sizes, showing NIR-II signal acquired from both sides of the brain slice, demonstrating the ability of the microscope system to image through tissues up to ≈300 µm deep. Same scale bar applies to all images.

SWNT-labeled slices could be used as a correlative measure of brain tissue morphology. Specifically, Huntington's Disease (HD) brain tissue has been previously been found to contain Huntingtin protein aggregates, which increases the tortuosity of the brain tissue microenvironment and possibly contributes to the motor deficits in advanced HD.[50] To this end, we labeled 300 µm brain slices generated from C57BL/6 Mice with SWNT, and also labeled 300 µm brain slices from R6/2 mouse models genotyped to confirm HD. By imaging these SWNT-labeled brain tissue slices, we sought to examine if we could utilize two-photon power laws to quantitatively differentiate healthy brain tissue from HD afflicted brain tissue (**Figure** 5a,b). Figure S7a–c (Supporting Information) show differential power laws in all slices, however the power law scalings are more significantly more highly varied in the HD brain slice compared to the wild type brain slice (Figure 5c). These results suggest two-photon NIR imaging combined with power law analyses could provide a quantitative analytical method to distinguish brain slices of
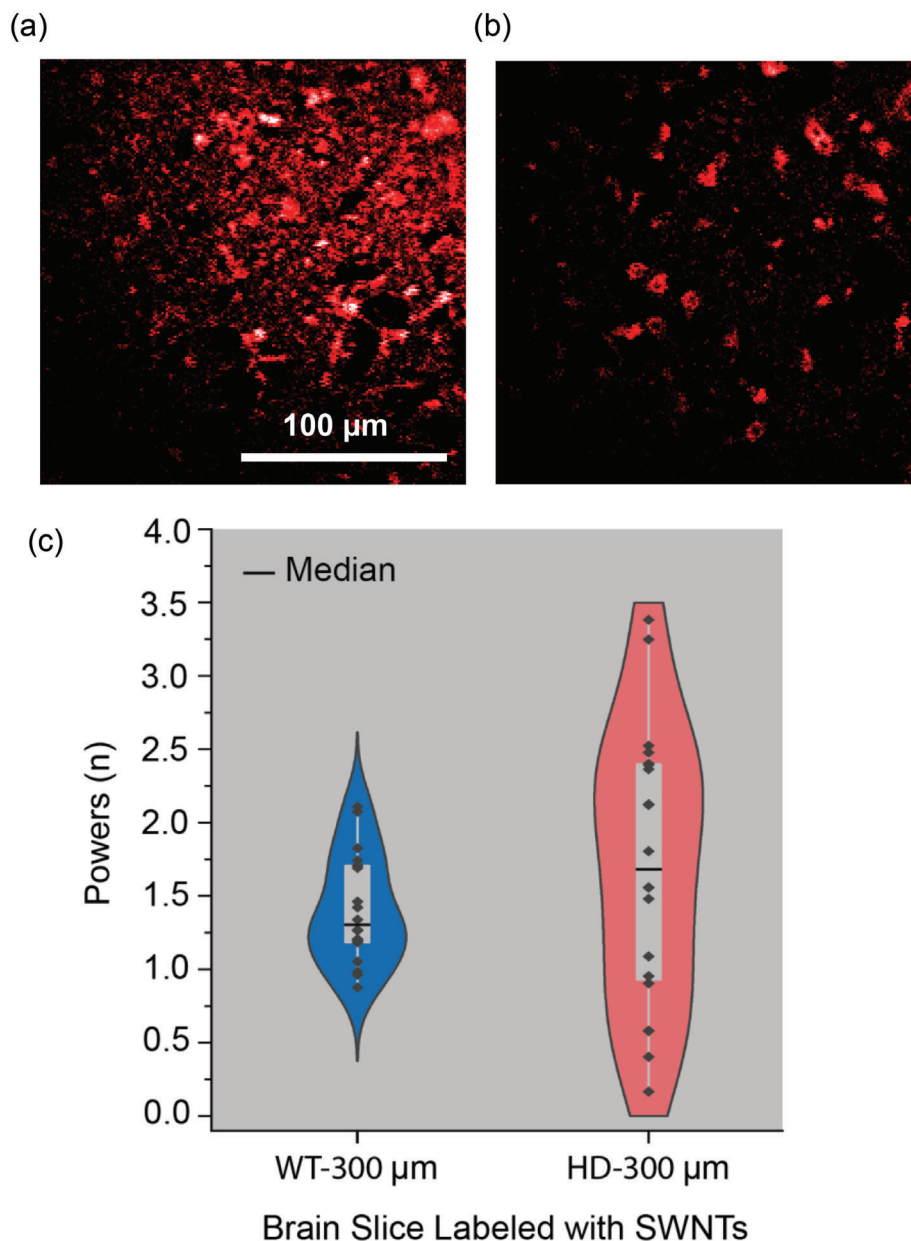
ADVANCED
SCIENCE NEWS

www.advancedsciencenews.com

ADVANCED
FUNCTIONAL
MATERIALS

www.afm-journal.de

Figure 5. Power law analysis of brain slices to measure tissue heterogeneity. Representative dual infrared two-photon image of a a) 300 µm brain slice generated from C57BL/6 Mice with SWNT, and b) a 300 µm brain slice generated R6/2 mouse models of Huntington's Disease (HD). Same scale bar applies to both (a) and (b). c) Corresponding two-photon power laws obtained from SWNT-labeled WT (blue) or HD (red) mouse brain slices. Power laws were calculated from selected ROIs from 1 WT and HD mouse brain slices. The colored region represents the distribution of the datapoints.

different tissue morphologies, based on extracellular space microstructure, such as those afflicted with late-stage HD from wild type brain slices.

2.5. Two-Photon Imaging of SWNT-Labeled Plant Tissue Reveals Deeper Tissue Imaging and Detects Zero Background Autofluorescence

Fluorescence imaging in plants is also critical to understanding plant structure and physiology. In addition to the canonical challenges to accomplishing fluorescence imaging in biological tissues, plants contain high concentrations of chlorophyll pigments which exhibit autofluorescence broadly through the visible and short-wavelength NIR spectrum.[51] These photophysical features unique to plant tissues have made fluorescence imaging in plants particularly difficult to accomplish. Specifically, plant-specific autofluorescence molecules such as chlorophylls and optically dense tissues diminish the clarity of imaging and limit the imaging depth to the outermost surface of plant leaves, motivating us to assess whether NIR-II two-photon microscopy could be used to image the morphology of leaf tissues. To determine the

**ADVANCED
SCIENCE NEWS**
www.advancedsciencenews.com

**ADVANCED
FUNCTIONAL
MATERIALS**
www.afm-journal.de

potential of our platform for in vivo plant leaf imaging, we infiltrated a *Nicotiana benthamiana* plant leaf of 180 μm thickness with (GT)$_{15}$-DNA-functionalized SWNTs which localize to the plant interstitial space and obtained z-stack images with 20 μm step sizes through the full leaf tissue depth (**Figure 6a,b**). We employed (GT)$_{15}$-SWNT for this purpose to have better background fluorescence intensity than (GT)$_6$-SWNT.[49] The images obtained at different optical z sections clearly resolve plant internal organs, notably the outline of plant stomata, cells, and veins, through the full leaf tissue at depth of up to 120 μm. The fact that the outline of the internal plant leaf organs is distinctly observable without a noticeable contribution from out-of-focus light demonstrates the capability of our NIR two-photon microscope to minimize chlorophyll autofluorescence from the acquired tissue image. As a control, no fluorescence signal is detected from a water-infiltrated leaf, confirming the minimal-background nature of our NIR two-photon imaging approach (Figure 6c, left). Moreover, fluorescence background from chlorophyll pigments in the leaf, and scattering of leaf tissues, is evident with NIR 1 photon microscopy (Figure 6c, middle) and with visible wavelength confocal microscopy (Figure 6c, right). However, NIR two-photon microscopy shows zero background autofluorescence despite the broad absorption and fluorescence emission spectrum of chlorophyll a and b pigments in plants.[52] These results further highlights the ability of our platform to minimize autofluorescence utilizing exclusively longer NIR excitation and emission wavelengths.

To determine the maximum imaging depth in plants, we infiltrated both sides of a plant leaf with NIR-emitting (GT)$_{15}$-SWNTs to ensure both sides of the leaf were labeled with NIR emitters and repeated the imaging procedure utilized for brain slice z-stack acquisition (Figure 6b). We acquired NIR signal and recorded images starting from the top of the leaf, through the full leaf thickness. We lost signal while traveling through the thickness of the leaf at ≈120–140 μm depth and did not re-gain signal when reaching to the other side of the leaf. While this demonstrates the imaging depth in plants is not as high as brain slices, the NIR two-photon platform can image plant internal organs at depths up to ≈120 μm with minimal blur and contribution from autofluorescing molecules. The shorter maximal depth achieved in plant leaves can be attributed to the substantial absorption of emission photons by biomolecules such as chlorophylls which are absent in brain tissue. These experimental results are corroborated by our simulation results demonstrating the disproportionately larger impact of absorption over scattering on the emission signal-to-noise in two-photon microscopy. We anticipate the depth of imaging in plants can be substantially improved in the future by using longer excitation wavelength lasers and chirality-pure SWNT samples emitting at longer NIR-II wavelengths.

3. Conclusion

Achieving high spatial resolution fluorescence imaging in biological tissues including brain and plant tissues is challenged by photon attenuation in both, and high autofluorescence of the latter. Canonical approaches to achieving deep-tissue imaging include near-infrared epifluorescence microscopy or multiphoton microscopy approaches, which optimize tissue transmission of either emission or excitation photons, respectively. Moreover, lit-

tle is known about the relative contributions of photon absorption versus scattering fates in the imaging outcomes of photons within biological tissues. In this work, we developed a Monte Carlo simulation framework to study the effects of photon absorption versus scattering on photon attenuation in simulated brain tissue. Surprisingly, we found that photon absorption contributes disproportionately over photon scattering to poor imaging quality by a surprisingly large margin of over 130-fold.

Based on our simulations, we designed a dual-infrared two-photon fluorescence microscope that enables both excitation and emission in the NIR-II window through an anti-stokes shift with a pulsed femtosecond laser to image fluorophores that can be excited and emit in the NIR-II region, while avoiding the 1350–1550 nm wavelength range in which photons are susceptible to absorption by water. We also quantified the X-Y and Z spatial resolutions of our system to be 0.92 and 6 μm, respectively.

To confirm the two-photon absorption process, we acquired the emission signal by varying excitation power from fluorescence SWNT emitters incorporated into an agarose gel and observed differential power laws varying between 1 and 2 depending on SWNT dispersion homogeneity, suggesting SWNT aggregation states can be quantified with two-photon microscopy. We posit that the differential power law of 2 expected in two-photon excitation are due to SWNT-SWNT charge transfer interactions, and as a result, are seen more commonly in aggregated than highly dispersed fluorophore samples.

Finally, to demonstrate the potential of our system in simultaneously enhancing the depth and spatial resolution of fluorescence imaging, we labeled both sides of brain slices and plant leaves with DNA-functionalized SWNT emitters and acquired z-stack images of these tissues. The system achieved ≈300 μm imaging depth in brain slices and ≈120 μm imaging depth in plant leaves. The lower imaging depth of the latter is attributable to the substantial photon absorption by molecules such as plant chlorophylls and confirms the disproportionately large contribution of absorption to imaging quality attenuation. Furthermore, the lack of any fluorescence signal detected in water-infiltrated leaf samples suggests that our technique successfully eliminates the issue of background excitation in highly autofluorescent tissues. The differential maximal imaging depth in brain versus plant tissues corroborates the results achieved with our Monte Carlo simulations and highlights the largely disproportionate contributions of photon absorption relative to scattering in determining imaging quality. In sum, our paper addresses the lack of microscopy hardware capable of capturing both excitation and emission channels in the near-infrared, to achieve all-infrared imaging. Application of our SWNT/NIR two-photon microscopy to visualize neuromodulation with high spatiotemporal resolution, as shown by one-photon microscopy,[12] is an exciting extension of this work. Although two-photon acquisition often compromises temporal resolution, our current system is, in principle, sufficient to image the ≈10 s long process of dopamine modulation in living brain tissue. While SWNT were used as a proof-of-principle fluorophore for this work, new developments in near-infrared fluorophores and fluorescent proteins could enable future all-infrared imaging capabilities that are specific to cells or biological structures. Near-infrared organic fluorophores can be used to tag biological structures and tissues, whereas near-infrared proteins can be genetically targeted for expression in
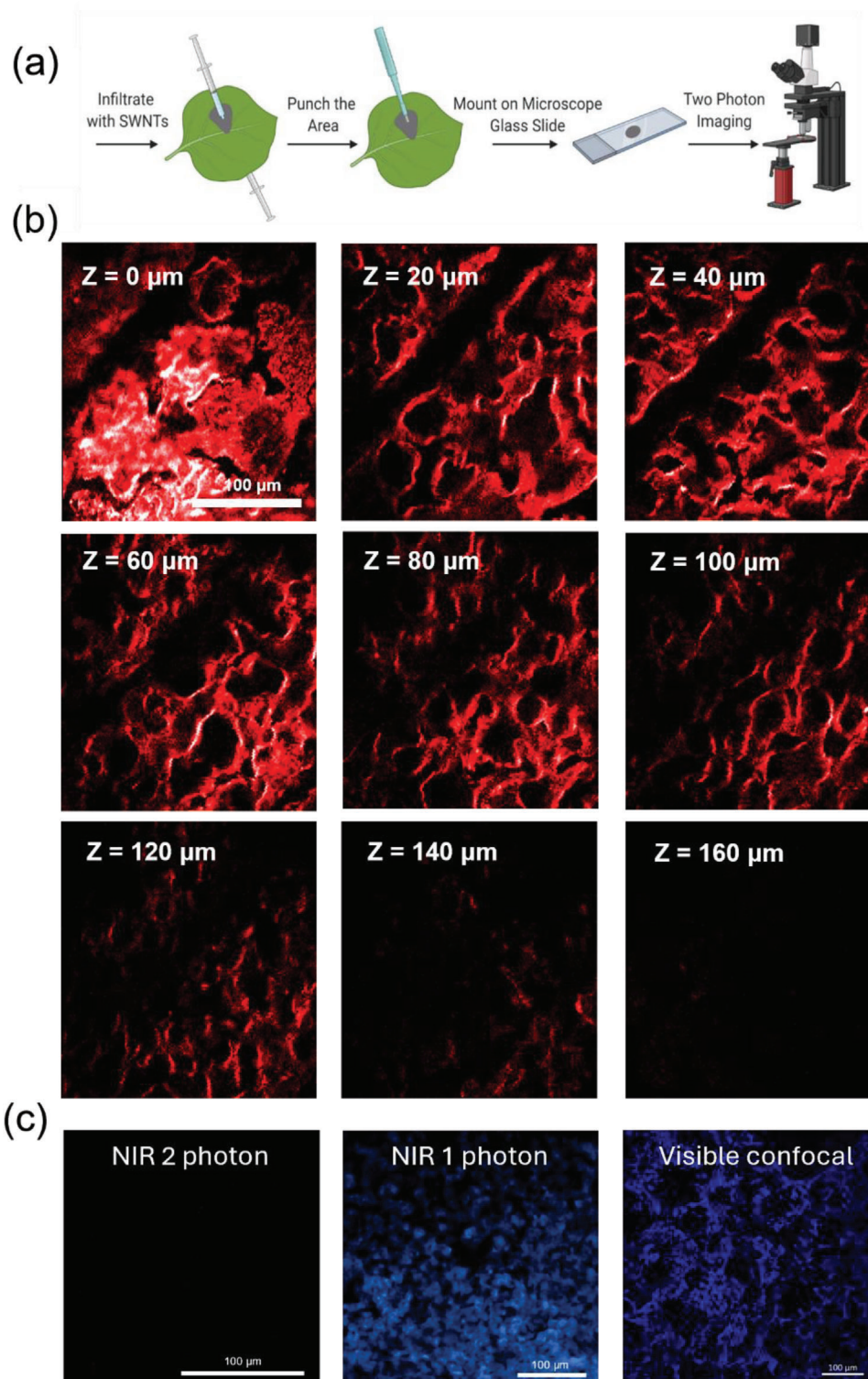
**ADVANCED
SCIENCE NEWS**

www.advancedsciencenews.com

*ADVANCED
FUNCTIONAL
MATERIALS*

www.afm-journal.de

Figure 6. Imaging a plant leaf labeled with SWNT emitters at both sides. a) Schematic representation of plant leaf infiltration with SWNTs. Same scale bar applies to all images. b) Imaging a 180 µm *Nicotiana benthamiana* plant leaf labeled with SWNT emitters on both surfaces A z-stack was acquired with 20 µm step sizes, indicating NIR-II at depth up to ≈120 µm. c) Comparison of fluorescence background in *Nicotiana benthamiana* plant leaves across imaging methods. *Nicotiana benthamiana* plant leaves infiltrated with only a buffer solution and imaged with (left) NIR two-photon microscopy (190 mW/cm^2); (middle) NIR single-photon epifluorescence microscopy with a 950 nm long-pass filter (160 mW/cm^2); (right) visible confocal microscopy with a 652–728 nm band pass filter.

**ADVANCED
SCIENCE NEWS**

www.advancedsciencenews.com

**ADVANCED
FUNCTIONAL
MATERIALS**

www.afm-journal.de

specific cell types for improved imaging quality. These future applications are supported by our microscopy development results herein, showing that our dual NIR-II two-photon imaging system demonstrates a notable improvement in imaging spatial resolution compared to current single photon and multiphoton imaging approaches, with superior deep-tissue imaging quality relative to single-photon near-infrared imaging.

Lastly, we find that NIR-II two-photon microscopy power laws are dependent on SWNT fluorophore aggregation state, a feature that is useful in quantifying the aggregation state of labeled tissues. We leverage this feature to distinguish Huntington's Disease brain tissue from wildtype by labeling brain slices with SWNT fluorophores and performing in-tissue imaging to distinguish diseased from wildtype tissues based on SWNT labeling homogeneity. In this work, we elected to demonstrate NIR two-photon imaging in brain tissues and plant tissues. The former provides a desirable biological tissue in which to achieve deep-tissue imaging, largely due to the depth of this biological organ and therefore the need to develop techniques to image deeper into this tissue. The latter provides an excellent example of a biological tissue that is rich in endogenous chromophores, chlorophyll pigments, that cause broad-spectrum photoabsorption and compromise the ability to image plant tissues, even with red-shifted fluorophores. Therefore, by imaging in both of these tissues, we provide proof-of-concept data suggestive of broad utility of NIR two-photon microscopy across diverse species. We therefore anticipate that our NIR two-photon microscope would also enable imaging of other biological tissues that have been challenging to access using conventional microscopy techniques, for instance: imaging in highly-pigmented blood biofluids, imaging in bone samples, and deep-tissue subcutaneous imaging. Thus, our results suggest that NIR-II two-photon microscopy presents an exciting platform for minimal-background imaging of biological tissues, potentiating its use to study tissue structure and morphology with micron-scale spatial resolution.

4. Experimental Section

Simulation Methods: The architecture and structure of simulation involved calculating 300 000 individual photon trajectories from the focal point of the objective toward a detector. At each step (100 nm grain size) of the simulation the chance of photon scattering was applied and, if scattered, the angle was calculated using the scattering anisotropy (g or hg) of brain tissue for NIR wavelengths (g = 0.92) and the equation:[53,54]

$$D\,(g, \theta) = \frac{1-g^2}{2\sqrt{2}}\left(1 + g^2 - 2g\cos\theta\right)^{-3/2} \quad (5)$$

Only scattering coefficient and focal point depth in tissue were varied, as absorbance and objective NA did not affect emission photon trajectories. The probability of scattering occurring over some length, L, governed by the equation $P_S\,(\mu_S, L) = 1 - e^{-\mu_S L}$. Scattering events were probabilistically generated for every step of travel. This simulation grain within this manuscript was 0.1 μm. This value was smaller than the wavelength of light used and smaller than the diameter of any axon or dendritic spine that might cause scattering in brain tissue, suggesting that finer simulation grains would be unnecessary. Next a range of detection conditions were applied to the database of trajectories, applying detection conditions

Table 1. List of the parameters and ranges of values used in the simulation of emission photons exiting scattering and absorbing media.

Variable	Symbol	Range	Step
Simulation Grain	L	0.1 μm	–
Anisotropy	g	0.92	–
Scattering Coefficient	μ_S	0, 0.1–10	x10^0.25
Absorption Coefficient	μ_A	0, 0.01–10	x10^0.25
Depth	D	0–2.5 mm	0.1 mm
Working Distance	WD	1–3.0 mm	0.25 mm
Numerical Aperture	NA	0.8–1.2	0.05

dependent on absorption coefficients, and the WD and NA of the objective. Emission photon trajectories were flagged as detected if they satisfied conditions set by the NA, WD, and trajectory position and vector upon exiting the simulated media (Figure 1a) To be detected, the exit trajectory must intercept the objective and the trajectory azimuthal angle must be less than a critical angle calculated from the NA of the objective. (**Table 1**)

Preparation of the Surface-Functionalized SWNT Emitters: Single-walled carbon nanotubes produced by the HiPco process (Nanointegris) were used throughout the study. For DNA functionalization, 1 mg of raw nanotubes was added to 2 mg of desalted (GT)n (n = 6 or 15) oligonucleotide (Integrated DNA Technologies, standard desalting) in a microcentrifuge tube with 1 mL of 0.1 M NaCl (Sigma-Aldrich). For surfactant functionalization, 1 mg of raw nanotubes were mixed with 1 mL of a 1% solution of an anionic surfactant sodium deoxycholate (SDC, Sigma Aldrich). The mixtures were then ultrasonicated using a 3 mm tapered microtip (Sonics Vibracell; Sonics & Materials) for 30 min at 40% amplitude, in a 0 °C temperature-controlled microcentrifuge tube holder. After sonication, the dispersion was centrifuged for 30 min at 15 000 rpm, and the top 80% of the supernatant was extracted to avoid recovering bundled or otherwise un-suspended SWNT material. The SWNT concentration was determined with a UV/Vis/NIR spectrophotometer, using the extinction coefficient of $A_{910} = 0.02554$ L/(mg cm). For special characterization of the microscope, PbS/CdS QDs were synthesized, following the procedure as described previously.[55]

Acute Slice Preparation and SWNT Labeling: The C57BL/6 strain male and female mice (60 days old) were group-housed after weaning at postnatal day 21 (P21) and kept with nesting material on a 12:12 light cycle. For the HD studies, male B6CBA-Tg(HDexon1)62Gpb/3J mice (R6/2 mice) were procured from Jackson Labs. At 6 weeks, male R6/2 mice were with 10-week-old female C57BL/6 mice. 3-week old pups were weaned and genotyped for the HD fragment. All animal procedures were approved by the University of California Berkeley Animal Care and Use Committee. To prepare acute brain slices, mice were injected ketamine/xylazine cocktail via intraperitoneal for deep anesthetization. Transcranial perfusion was performed using ice-cold cutting buffer (119 mM NaCl, 26.2 mM NaHCO₃, 2.5 mM KCl, 1 mM NaH₂PO₄, 3.5 mM MgCl₂, 10 mM glucose, and 0 mM CaCl2), followed by rapid brain extraction. The cerebellum and other connective tissues were trimmed using a razor blade, and the brain was mounted onto the cutting stage of a vibratome (Leica VT1200 S). Coronal slices with 300 μm thickness including the dorsal striatum were prepared. To label with SWNT fluorescent emitters, slices were incubated with 5 mL of oxygen saturated ACSF in a small volume brain slice incubation chamber (Scientific Systems Design Inc., AutoMate Scientific). 100 μL of the (GT)₆-SWNT dispersion was carefully added to one side of the slice, and the slice was incubated in this solution for 15 min. To label the other side of the slice, the procedure was repeated by carefully flipping the slice and adding the SWNT dispersion to the other side. The slice was subsequently recovered and rinsed in oxygen-saturated ACSF to wash off SWNTs that did not localize into the brain tissue. The rinsing step was repeated by transferring the slice through three wells of a 24-well plate (5 s in each well). The slices were then mounted onto microscope glass slides for imaging. For one-photon imaging, a labeled slice was placed on a glass

**ADVANCED
SCIENCE NEWS**

www.advancedsciencenews.com

**ADVANCED
FUNCTIONAL
MATERIALS**

www.afm-journal.de

coverslip (#3305, thickness 0.17 mm, ThermoFisher Scientific) and covered by 50 µL of ACSF. The brain slice was then imaged on a one-photon epifluorescence microscope with a Ninox VIS-SWIR 640 (Rapter Photonics) detector. The sensors were excited with 721 nm and the emitted fluorescence signal was collected through a 900 nm longpass filter. The image was collected at the focus which corresponds to the backside of the brain slice.

Plant Leaf Preparation and SWNT Labeling: A 100 µL solution of the $(GT)_{15}$-SWNTs was infiltrated on both surfaces of healthy and fully developed *Nicotiana benthamiana* leaves with a 1-ml needleless syringe with caution not to damage the leaf. The infiltrated area was then punched out and mounted onto a microscope glass slide for two-photon imaging. For the visible confocal microscopy, standard confocal microscopy experiments were conducted with leaf discs excised from 5-week-old *Nicotiana benthamiana* plants. Images were collected at the at the CRL Molecular Imaging Center, RRID:SCR_017852, with a Zeiss LSM880 laser scanning confocal microscope with a Fluar 5x/0.25 M27 objective. Leaf discs were placed up-side down, mounted in between #1.5 cover glass with a drop of 50% glycerol, and imaged on the abaxial side. Chloroplast autofluorescence was acquired by excitation with a 635 nm laser with emission collected between 652 and 728 nm with the pinhole aperture set to 1 Airyunit. Z-stacks were transformed into maximum intensity projections using Zen Blue software.

Data Analysis and Figures: Data analyses were performed with OriginPro and schematic figures were created with BioRender.com.

Supporting Information

Supporting Information is available from the Wiley Online Library or from the author.

Conflict of Interest

The authors declare no conflict of interest.

Author Contributions

M.M.S. and S.N. contributed equally to this work and may change the order of the co-contributor author list when presenting or reporting on this work. I.R.M. and M.L. conceived and designed the project. I.R.M. designed and carried out the Monte Carlo Simulations. I.R.M. and M.M.S. built the microscope and carried out the two-photon microscopy imaging. S.J.Y. and S.N. prepared brain slice samples and carried out one-photon microscopy imaging. H.S. carried out the visible confocal microscopy. S.N. finalized the manuscript and completed the revision processes. M.P.L. provided technical guidance, research prioritization, and significant manuscript writing input. All authors provided editorial guidance for the manuscript.

Data Availability Statement

The data that support the findings of this study are available from the corresponding author upon reasonable request.

[1] G. Hong, A. L. Antaris, H. Dai, *Nat. Biomed. Eng.* **2017**, *1*, 0010.
[2] S. Zhu, R. Tian, A. L. Antaris, X. Chen, H. Dai, *Adv. Mater.* **2019**, *31*, 1900321.
[3] M. Zhang, J. Yue, R. Cui, Z. Ma, H. Wan, F. Wang, S. Zhu, Y. Zhou, Y. Kuang, Y. Zhong, D.-W. Pang, H. Dai, *Proc. Natl. Acad. Sci. USA* **2018**, *115*, 6590.
[4] F. Xia, M. Gevers, A. Fognini, A. T. Mok, B. Li, N. Akbari, I. E. Zadeh, J. Qin-Dregely, C. Xu, *ACS Photonics* **2021**, *8*, 2800.
[5] Y. Hontani, F. Xia, C. Xu, *Sci. Adv.* **2021**, *7*, eabf3531.
[6] G. Hong, S. Diao, J. Chang, A. L. Antaris, C. Chen, B. Zhang, S. Zhao, D. N. Atochin, P. L. Huang, K. I. Andreasson, C. J. Kuo, H. Dai, *Nat. Photonics* **2014**, *8*, 723.
[7] G. Hong, Y. Zou, A. L. Antaris, S. Diao, D. Wu, K. Cheng, X. Zhang, C. Chen, B. Liu, Y. He, J. Z. Wu, J. Yuan, B. Zhang, Z. Tao, C. Fukunaga, H. Dai, *Nat. Commun.* **2014**, *5*, 4206.
[8] H. Wan, H. Du, F. Wang, H. Dai, *Adv. Funct. Mater.* **2019**, *29*, 1900566.
[9] G. Hong, S. Diao, A. L. Antaris, H. Dai, *Chem. Rev.* **2015**, *115*, 10816.
[10] F. Wang, Z. Ma, Y. Zhong, F. Salazar, C. Xu, F. Ren, L. Qu, A. M. Wu, H. Dai, *Proc. Natl. Acad. Sci. USA* **2021**, *118*, 2023888118.
[11] S. J. Yang, J. T. Del Bonis-O'Donnell, A. G. Beyene, M. P. Landry, *Nat. Protoc.* **2021**, *16*, 3026.
[12] A. G. Beyene, K. Delevich, J. T. Del Bonis-O'Donnell, D. J. Piekarski, W. C. Lin, A. W. Thomas, S. J. Yang, P. Kosillo, D. Yang, G. S. Prounis, L. Wilbrecht, M. P. Landry, *Sci. Adv.* **2019**, *5*, eaaw3108.
[13] J. M. Girkin, *J. Phys. D Appl. Phys.* **2003**, *36*, R250.
[14] J. T. D. Bonis-O'Donnell, R. H. Page, A. G. Beyene, E. G. Tindall, I. R. McFarlane, M. P. Landry, *Adv. Funct. Mater.* **2017**, *27*, 1702112.
[15] Y. Zhong, Z. Ma, F. Wang, X. Wang, Y. Yang, Y. Liu, X. Zhao, J. Li, H. Du, M. Zhang, Q. Cui, S. Zhu, Q. Sun, H. Wan, Y. Tian, Q. Liu, W. Wang, K. C. Garcia, H. Dai, *Nat. Biotechnol.* **2019**, *37*, 1322.
[16] W. Wang, Z. Ma, S. Zhu, H. Wan, J. Yue, H. Ma, R. Ma, Q. Yang, Z. Wang, Q. Li, Y. Qian, C. Yue, Y. Wang, L. Fan, Y. Zhong, Y. Zhou, H. Gao, J. Ruan, Z. Hu, Y. Liang, H. Dai, *Adv. Mater.* **2018**, *30*, 1800106.
[17] H. Wan, J. Yue, S. Zhu, T. Uno, X. Zhang, Q. Yang, K. Yu, G. Hong, J. Wang, L. Li, Z. Ma, H. Gao, Y. Zhong, J. Su, A. L. Antaris, Y. Xia, J. Luo, Y. Liang, H. Dai, *Nat. Commun.* **2018**, *9*, 1171.
[18] Y. Song, S. Zhu, B. Yang, *RSC Adv.* **2014**, *4*, 27184.
[19] J. Du, N. Xu, J. Fan, W. Sun, X. Peng, *Small* **2019**, *15*, 1805087.
[20] Y. Yomogida, T. Tanaka, M. Zhang, M. Yudasaka, X. Wei, H. Kataura, *Nat. Commun.* **2016**, *7*, 12056.
[21] A. L. Antaris, J. T. Robinson, O. K. Yaghi, G. Hong, S. Diao, R. Luong, H. Dai, *ACS Nano* **2013**, *7*, 3644.
[22] G. Hong, J. C. Lee, J. T. Robinson, U. Raaz, L. Xie, N. F. Huang, J. P. Cooke, H. Dai, *Nat. Med.* **2012**, *18*, 1841.
[23] K. Welsher, Z. Liu, S. P. Sherlock, J. T. Robinson, Z. Chen, D. Daranciang, H. Dai, *Nat. Nanotechnol.* **2009**, *4*, 773.
[24] K. Welsher, S. P. Sherlock, H. Dai, *Proc. Natl. Acad. Sci. USA* **2011**, *108*, 8943.

[25] W. Zong, R. Wu, S. Chen, J. Wu, H. Wang, Z. Zhao, G. Chen, R. Tu, D. Wu, Y. Hu, Y. Xu, Y. Wang, Z. Duan, H. Wu, Y. Zhang, J. Zhang, A. Wang, L. Chen, H. Cheng, *Nat. Methods* **2021**, *18*, 46.

[26] S. Celli, M. L. Albert, P. Bousso, *Nat. Med.* **2011**, *17*, 744.

[27] G. C. R. Ellis-Davies, *ACS Chem. Neurosci.* **2011**, *2*, 185.

[28] F. Helmchen, W. Denk, *Nat. Methods* **2005**, *2*, 932.

[29] W. Zong, R. Wu, M. Li, Y. Hu, Y. Li, J. Li, H. Rong, H. Wu, Y. Xu, Y. Lu, H. Jia, M. Fan, Z. Zhou, Y. Zhang, A. Wang, L. Chen, H. Cheng, *Nat. Methods* **2017**, *14*, 713.

[30] D. R. Miller, J. W. Jarrett, A. M. Hassan, A. K. Dunn, *Curr. Opin. Biomed. Eng.* **2017**, *4*, 32.

[31] G. Qian, B. Dai, M. Luo, D. Yu, J. Zhan, Z. Zhang, D. Ma, Z. Y. Wang, *Chem. Mater.* **2008**, *20*, 6208.

[32] F. Yang, M. Wang, D. Zhang, J. Yang, M. Zheng, Y. Li, *Chem. Rev.* **2020**, *120*, 2693.

[33] Y. Luo, E. D. Ahmadi, K. Shayan, Y. Ma, K. S. Mistry, C. Zhang, J. Hone, J. L. Blackburn, S. Strauf, *Nat. Commun.* **2017**, *8*, 1413.

[34] M. M. Safaee, M. Gravely, D. Roxbury, *Adv. Funct. Mater.* **2021**, *31*, 2006254.

[35] R. Nißler, O. Bader, M. Dohmen, S. G. Walter, C. Noll, G. Selvaggio, U. Groß, S. Kruss, *Nat. Commun.* **2020**, *11*, 5995.

[36] M. Kim, C. Chen, P. Wang, J. J. Mulvey, Y. Yang, C. Wun, M. Antman-Passig, H.-B. Luo, S. Cho, K. Long-Roche, L. V. Ramanathan, A. Jagota, M. Zheng, Y. Wang, D. A. Heller, *Nat. Biomed. Eng.* **2022**, *6*, 267.

[37] R. L. Pinals, F. Ledesma, D. Yang, N. Navarro, S. Jeong, J. E. Pak, L. Kuo, Y.-C. Chuang, Y.-W. Cheng, H.-Y. Sun, M. P. Landry, *Nano Lett.* **2021**, *21*, 2272.

[38] N. M. Bardhan, D. Ghosh, A. M. Belcher, *Nat. Commun.* **2014**, *5*, 4918.

[39] V. Zubkovs, A. Antonucci, N. Schuergers, B. Lambert, A. Latini, R. Ceccarelli, A. Santinelli, A. Rogov, D. Ciepielewski, A. A. Boghossian, *Sci. Rep.* **2018**, *8*, 13770.

[40] S. Aota, N. Akizuki, S. Mouri, K. Matsuda, Y. Miyauchi, *Appl. Phys. Express* **2016**, *9*, 045103.

[41] J. G. Duque, A. N. G. Parra-Vasquez, N. Behabtu, M. J. Green, A. L. Higginbotham, B. K. Price, A. D. Leonard, H. K. Schmidt, B. Lounis, J. M. Tour, S. K. Doorn, L. Cognet, M. Pasquali, *ACS Nano* **2010**, *4*, 3063.

[42] J. G. Duque, C. G. Densmore, S. K. Doorn, *J. Am. Chem. Soc.* **2010**, *132*, 16165.

[43] C. Xu, W. W. Webb, *J. Opt. Soc. Am. B* **1996**, *13*, 481.

[44] F. Wang, G. Dukovic, L. E. Brus, T. F. Heinz, *Science* **2005**, *308*, 838.

[45] M. L. Zaccaria, F. Di Tommaso, A. Brancaccio, P. Paggi, T. C. Petrucci, *Neuroscience* **2001**, *104*, 311.

[46] G. Brückner, W. Härtig, J. Kacza, J. Seeger, K. Welt, K. Brauer, *Journal of Neurocytology* **1996**, *25*, 333.

[47] A. G. Godin, J. A. Varela, Z. Gao, N. Danné, J. P. Dupuis, B. Lounis, L. Groc, L. Cognet, *Nat. Nanotechnol.* **2017**, *12*, 238.

[48] C. Paviolo, L. Cognet, *Neurobiol. Dis.* **2021**, *153*, 105328.

[49] A. G. Beyene, A. A. Alizadehmojarad, G. Dorlhiac, N. Goh, A. M. Streets, P. Král, L. Vukovic, M. P. Landry, *Nano Lett.* **2018**, *18*, 6995.

[50] M. A. Johnson, M. Villanueva, C. L. Haynes, A. T. Seipel, L. A. Buhler, R. M. Wightman, *J. Neurochem.* **2007**, *103*, 2102.

[51] T. T. S. Lew, V. B. Koman, K. S. Silmore, J. S. Seo, P. Gordiichuk, S.-Y. Kwak, M. Park, M. C.-Y. Ang, D. T. Khong, M. A. Lee, M. B. Chan-Park, N.-H. Chua, M. S. Strano, *Nat. Plants* **2020**, *6*, 404.

[52] T. Takahashi, *Molecules* **2019**, *24*, 4441.

[53] Y. Pu, J. Chen, W. Wang, R. R. Alfano, *Basic Optical Scattering Parameter of the Brain and Prostate Tissues in the Spectral Range of 400–2400 Nm*, Elsevier, Amsterdam, Netherlands **2018**.

[54] F. Bevilacqua, D. Piguet, P. Marquet, J. D. Gross, B. J. Tromberg, C. Depeursinge, *Appl. Opt.* **1999**, *38*, 4939.

[55] S. Jeong, J. Song, W. Lee, Y. M. Ryu, Y. Jung, S.-Y. Kim, K. Kim, S. C. Hong, S. J. Myung, S. Kim, *Nano Lett.* **2017**, *17*, 1378.